J. Fluid Mech. (1997), *vol.* 330, *pp.* 349–374

Direct numerical simulation of turbulent flow over a backward-facing step

By HUNG LE[1], PARVIZ MOIN[1] AND JOHN KIM[2]

[1]Department of Mechanical Engineering, Stanford University, Stanford, CA 94305, USA

[2]Department of Mechanical, Aerospace and Nuclear Engineering, University of California, Los Angeles, Los Angeles, CA 90024, USA

(Received 14 March 1996 and in revised form 3 September 1996)

Turbulent flow over a backward-facing step is studied by direct numerical solution of the Navier–Stokes equations. The simulation was conducted at a Reynolds number of 5100 based on the step height h and inlet free-stream velocity, and an expansion ratio of 1.20. Temporal behaviour of spanwise-averaged pressure fluctuation contours and reattachment length show evidence of an approximate periodic behaviour of the free shear layer with a Strouhal number of 0.06. The instantaneous velocity fields indicate that the reattachment location varies in the spanwise direction, and oscillates about a mean value of $6.28h$. Statistical results show excellent agreement with experimental data by Jovic & Driver (1994). Of interest are two observations not previously reported for the backward-facing step flow: (*a*) at the relatively low Reynolds number considered, large negative skin friction is seen in the recirculation region; the peak $|C_f|$ is about 2.5 times the value measured in experiments at high Reynolds numbers; (*b*) the velocity profiles in the recovery region fall below the universal log-law. The deviation of the velocity profile from the log-law indicates that the turbulent boundary layer is not fully recovered at 20 step heights behind the separation.

The budgets of all Reynolds stress components have been computed. The turbulent kinetic energy budget in the recirculation region is similar to that of a turbulent mixing layer. The turbulent transport term makes a significant contribution to the budget and the peak dissipation is about 60% of the peak production. The velocity–pressure gradient correlation and viscous diffusion are negligible in the shear layer, but both are significant in the near-wall region. This trend is seen throughout the recirculation and reattachment region. In the recovery region, the budgets show that effects of the free shear layer are still present.

1. Introduction

Separation and reattachment of turbulent flows occur in many practical engineering applications, both in internal flow systems such as diffusers, combustors and channels with sudden expansions, and in external flows like those around airfoils and buildings. In these situations, the flow experiences an adverse pressure gradient, i.e. the pressure increases in the direction of the flow, which causes the boundary layer to separate from the solid surface. The flow subsequently reattaches downstream forming a recirculation bubble. Among the flow geometries used for the studies of separated

flows, the most frequently selected is the backward-facing step. Considerable work has been carried out on this flow due to its geometrical simplicity.

The effects of expansion ratio (ER) on the reattachment length were studied by Kuehn (1980), Durst & Tropea (1981), Ötügen (1991), and Ra & Chang (1990). The reattachment length was found to increased with ER in these studies. Armaly *et al.* (1983) studied the effect of Reynolds number on the reattachment length, X_r. They found that X_r increased with Reynolds number up to $Re \approx 1200$ (Reynolds number based on step height h and inlet free-stream velocity U_0), then decreased in the transitional range $1200 < Re < 6600$, and remained relatively constant when the flow became fully turbulent at $Re > 6600$. Their findings agreed well with experiments by Durst & Tropea (1981) and Sinha, Gupta & Oberai (1981). Other parameters affecting X_r were also investigated: upstream boundary layer profile (Adams, Johnston & Eaton 1984), inlet turbulence intensity (Isomoto & Honami 1989), and downstream duct angle (Westphal, Johnston & Eaton 1984).

Eaton & Johnston (1980), Westphal *et al.* (1984), Adams & Johnston (1985), and Driver & Seegmiller (1985) all measured the skin friction coefficient, C_f, on the step wall. Although there is a large variation in Reynolds number and expansion ratio among these experiments, all reported a high level of $|C_f|$ in the recirculation region. The present study showed that the peak value of $|C_f|$ can be significantly higher at low Reynolds numbers. This finding prompted a companion experimental investigation at the same Reynolds number and expansion ratio as the present numerical study (Jovic & Driver 1994).

Investigations of the flow velocity profiles and turbulence intensities in the recovery region were conducted by Bradshaw & Wong (1972), Kim, Kline & Johnston (1978), Westphal *et al.* (1984), and Adams *et al.* (1984). These experiments showed that, even though the mean streamwise velocity profiles were not fully recovered at more than 50 step heights behind the separation, a full recovery of the log-law profile near the wall was attained as early as 6 step heights after the reattachment.

Several numerical simulations of the backward-facing step flow were also conducted, but largely confined to two-dimensional calculations (Armaly *et al.* 1983; Durst & Pereira 1988; Kaiktsis, Karniadakis & Orszag 1991). Three-dimensional calculations were also performed by Kaiktsis *et al.* (1991) and by Friedrich & Arnal (1990) using the large-eddy simulation technique. The present direct simulation is the most detailed and extensive calculation of turbulent flow over a backward-facing step. It provides some insight into the unsteady characteristics of this flow as well as a database for turbulence modelling, containing up to third-order statistics and Reynolds stress budgets at all locations in the flow field.

2. Method

2.1. *Computational domain*

Figure 1 shows the schematic view of the flow domain used in the three-dimensional simulation. The computational domain consists of a streamwise length $L_x = 30h$, including an inlet section $L_i = 10h$ prior to the sudden expansion, vertical height $L_y = 6h$ and spanwise width $L_z = 4h$, where h is the step height. The coordinate system is placed at the lower step corner as shown in figure 1. The *mean* inflow velocity profile, $U(y)$, imposed at the left boundary $x = -L_i$ is a flat-plate turbulent boundary layer profile (Spalart 1988), with U_0 being the maximum mean inlet velocity. The

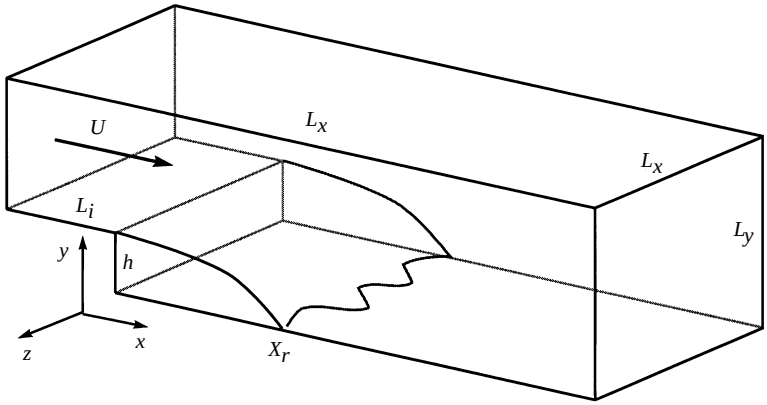

FIGURE 1. Backward-facing step flow configuration.

step-height Reynolds number is defined as $Re_h = U_0 h/\nu$, and the expansion ratio is $ER = L_y/(L_y - h)$.

To validate the computational results, a parallel experiment was conducted by Jovic & Driver (1994) at NASA Ames Research Center (hereinafter referred to as the "JD" experiment) which matches the current simulation in expansion ratio ($ER = 1.20$), boundary layer thickness at the step ($\delta_{99}/h = 1.20$) and Reynolds number ($Re_h \approx 5000$). The reader is referred to Jovic & Driver (1994) for a more detailed description. The computational results and JD data will be compared througout this report.

The governing equations are the Navier–Stokes and continuity equations for incompressible viscous flows:

$$\frac{\partial}{\partial t}u_i = -\frac{\partial}{\partial x_k}u_i u_k + \nu\frac{\partial^2}{\partial x_k \partial x_k}u_i - \frac{1}{\rho}\frac{\partial}{\partial x_i}p, \tag{2.1}$$

$$\frac{\partial}{\partial x_k}u_k = 0, \tag{2.2}$$

where the u_i are the velocity components, p the pressure, ν the kinematic viscosity, and ρ the density. The subscripts i, j, k take values of 1,2,3 to denote the streamwise (x), vertical (y) and spanwise (z) directions, respectively. All variables are non-dimensionalized by U_0 and h.

A staggered grid (Harlow & Welch 1965) is employed in the computations where the pressure is defined at the centre of the cell and velocity components on the cell surfaces. Uniform grid spacings are selected for the streamwise and spanwise directions. A total of 768 computational cells are used in the x-direction and 64 cells in the z-direction. In the vertical direction, a non-uniform mesh distribution is used with fine grid spacings near the lower wall and at the step. Details of the grid compression method are documented by Le & Moin (1994). The total number of computational cells in the vertical direction is 192, of which 70 are placed within the step ($y < h$). The grid spacings in the three directions in wall units are $\Delta x^+ \approx 10$, $\Delta y^+_{min} \approx 0.3$, $\Delta y^+_{max} \approx 31$, and $\Delta z^+ \approx 15$, respectively, based on the inlet boundary layer shear velocity, $u_{\tau 0}$.

Extensive grid-dependent studies on two- and three-dimensional simulations are conducted to ensure adequacy of the above grid spacings. These studies show that several flow characteristics are significantly affected by the streamwise grid spac-

ings. (*a*) Insufficient spatial resolution causes an otherwise steady flow to become quasi-periodic (Le & Moin 1994). Recent work by Gresho *et al.* (1993) has also independently shown that insufficient resolution will result in an unsteady numerical solutions in backward-facing step simulations. (*b*) For the Reynolds number considered in this study, a minimum of 512 streamwise cells in the post-expansion region ($\Delta x^+ \approx 10$ based on $u_{\tau 0}$) is required to adequately resolve the unsteady flow structures. A 10% reduction in the reattachment length is also observed as the number of cells is increased from 320 to 512. Further streamwise grid refinement does not result in significant improvements. (*c*) Vertical grid refinement is necessary at the step for the correct development of the near-wall turbulence in the entry section. The post-expansion flow characteristics are affected only by the vertical grid spacings at the bottom wall. The grid size at the step and bottom wall of $\Delta y^+_{min} \approx 0.3$ (based on $u_{\tau 0}$) is adequate for this purpose. (*d*) The spanwise resolution of 64 cells ($\Delta z^+ \approx 15$ based on $u_{\tau 0}$) appears to be sufficient for the Reynolds number considered. Doubling the spanwise grid cells does not improve the first-order statistics. However, examination of one-dimesional energy spectra indicates that higher spanwise resolution is desirable to resolve the small-scale structures at $y^+ < 10$.

2.2. *Boundary conditions*

A no-stress wall is applied at the upper boundary of the computational domain. The velocities at the no-stress wall are

$$v = 0, \qquad \frac{\partial u}{\partial y} = \frac{\partial w}{\partial y} = 0. \tag{2.3}$$

In the spanwise direction, the flow is assumed to be statistically homogeneous and periodic boundary conditions are used. No-slip boundary conditions are used at all other walls.

The mean inlet velocity profile, $U(y)$, is obtained from Spalart's (1988) boundary layer simulation at $Re_\theta = 670$, where θ is the momentum thickness. The boundary layer thickness is $\delta_{99} = 1.2h$. The corresponding step-height Reynolds number is $Re_h \approx 5100$. The time-dependent velocities prescribed at the inlet consist of $U(y)$ and the imposed fluctuations, $u_i'(y, z, t)$. Lee, Lele & Moin (1992) described a method of generating inflow fluctuations with a prescribed energy spectrum. However, their method is not readily applicable to the generation of inlet turbulence for the backward-facing step flow because of the inhomogeneity in the y-direction. The same basic method is thus applied in this study, but the resulting u_i' are scaled such that the calculated fluctuations conform to all four Reynolds stress components, $\overline{u'^2}$, $\overline{v'^2}$, $\overline{w'^2}$ and $\overline{u'v'}$, associated with the inlet boundary layer profile from Spalart (1988). Details of the method are described in Le & Moin (1994). The use of Lee *et al.*'s (1992) procedure ensures that the resulting signals do not contain excessive small-scale motions which would have resulted if simply random numbers were used to generate u', v' and w'.

Although this procedure gives a set of stochastic signals that satisfy a prescribed set of second-order statistics, the flow quickly loses its statistical characteristics within the first few step heights from the inlet (Le & Moin 1994), and slowly recovers after a transition length. This initial transition is due to the unphysical (structureless) inlet turbulence which was a result of the randomized phase angles in the Lee *et al.*'s (1992) method. A transition length of about $10h$ is required for the recovery of turbulent characteristics. In our calculations the mean flow reaches to within 6% of the target values of Spalart (1988) after approximately 7 step heights.

The exit boundary condition is the convective condition used by Lowery & Reynolds (1986) in numerical simulations of spatially evolving mixing layers. Pauley, Moin & Reynolds (1988) showed that, for unsteady problems, the convective boundary condition is suitable for moving vortical structures out of the computational domain. The time-dependent condition of any velocity component u_i at the exit plane ($x = L_x$) is taken as

$$\frac{\partial u_i}{\partial t} + U_c \frac{\partial u_i}{\partial x} = 0. \tag{2.4}$$

U_c is the convection velocity which is the constant mean exit velocity. Examination of several statistical quantities from three-dimensional simulations indicates that the most severe effects of the outflow boundary conditions on the flow statistics are confined to within one step height from the exit (Le & Moin 1994).

2.3. *Time advancement*

The governing equations are time-advanced using a semi-implicit method. The advancement scheme for the velocity components u_i is a compact-storage third-order Runge–Kutta scheme (Spalart 1987 and Spalart, Moser & Rogers 1991) which has an explicit treatment for the convective terms and implicit for the viscous term. The three-substep Runge–Kutta scheme is combined with the fractional step procedure (Kim & Moin 1985): the method of Le & Moin (1991) is used which allowed for the advancement of the velocity field through the substeps without satisfying the continuity equation at each Runge–Kutta substep. The velocities are projected onto the divergence-free field only at the last substep. The convective terms are modified to preserve the second-order accuracy of the scheme.

The Poisson equation for pressure is solved using a two-iteration *capacitance matrix* method developed by Schumann & Benner (1982). The reader is referred to Le & Moin (1994) for the detailed development of the capacitance matrix method which is tailored to the specific configuration and boundary conditions of the backward-facing step.

The time step in the current simulation is fixed at $\Delta t = 0.0018h/U_0$ which keeps the CFL number below 1.15. The algorithm requires approximately 13 mega-words of memory. Each time step uses 22 CPU seconds on the CRAY C-90, about 10 seconds of which is devoted to solving the Poisson equation. The efficiency rating of the program is approximately 450 mega-flops.

The total simulation time is $t_{total} = 382h/U_0$. Approximately 11 'flow-through' times (or $\approx 273h/U_0$) of the total simulation time is discarded to allow for the passage of initial transients. The 'flow-through' time here is defined as the convection time through the post-expansion section of $20h$ at the mean convective speed, $U_c \approx 0.8U_0$. The necessity of using a large initial transient period is due to the large residence time of fluid particles in the recirculation zone. The statistical data set, including the Reynolds stress budgets, is accumulated over the remaining time, $\Delta T_{ave} = 109h/U_0$ or 6070 samples (one sample at every 10 time steps).

3. Results and discussion

3.1. *Unsteady flow characteristics*

Friedrich & Arnal (1990) observed from their LES results that the free-shear layer emanating from the step had a vertical motion causing the reattachment location to oscillate. A low-frequency 'flapping' motion of the flow was also reported by Eaton &

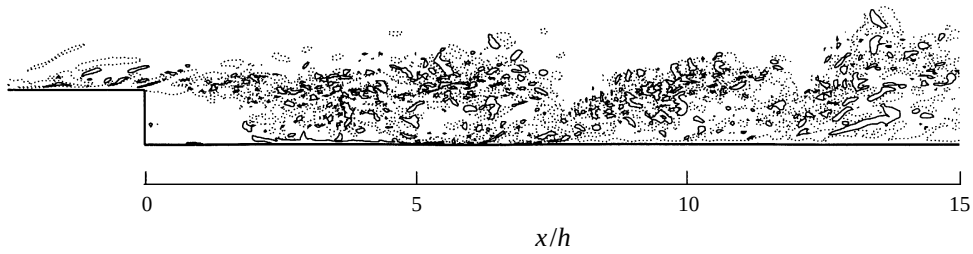

FIGURE 2. Instantanous spanwise vorticity (ω_z) contours: ····· , $-1.0U_0/h$ contours; ——— , $1.0U_0/h$ contours.

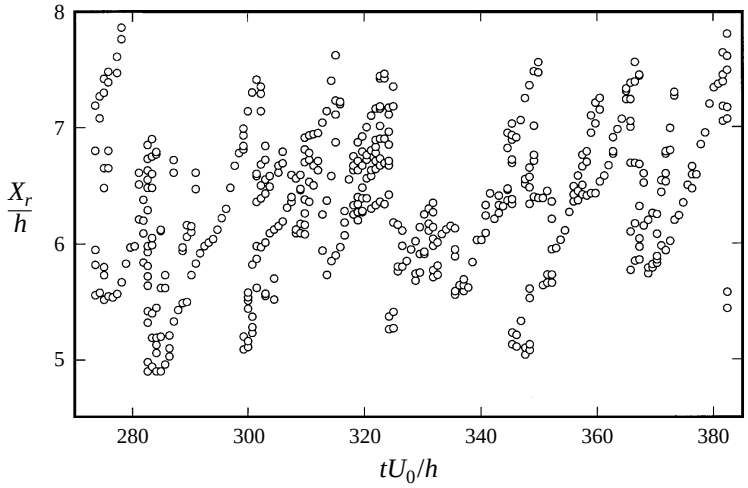

FIGURE 3. Motion of the spanwise-averaged reattachment locations.

Johnston (1980), and periodic vortical motions were observed by Driver, Seegmiller & Marvin (1983, 1987). In two-dimensional simulations at high Reynolds numbers, Le & Moin (1994) demonstrated this oscillatory motion with the spanwise vorticity contours. For the present three-dimensional simulation, the instantaneous spanwise vorticity contours at a selected (x, y)-plane are plotted in figure 2. There is an apparent large-scale roll-up of the shear layer extending to the reattachment region which is composed of many small, high-intensity counter-rotating vortices. The oscillatory flow behaviour is better observed by the motion of the reattachment location(s). Figure 3 displays the temporal trace of the reattachment locations which has a saw-tooth shape. Here, an instantaneous reattachment location is the location of zero C_f of the *spanwise-averaged* flow field. A likely scenario for the saw-tooth shape of the X_r *vs.* t plot is as follows. The shear layer rolls up forming a large-scale structure behind the step. As the large-scale structure grows, the reattachment location, X_r, travels downstream at a constant speed, indicated by the linear positive slopes in figure 3. The reattachment length then suddenly decreases indicating a detachment of the turbulent large-scale structure from the step. This movement of the turbulent vortices can be more accurately elucidated by studying pressure fluctuations; low-pressure regions have been shown to correspond to the centres of coherent vortices. The pressure fluctuations p' as a function of time at a location near the reattachment, $x/h = 6.0$ and $y/h = 0.055$, are shown in figure 4. Again, presented here are

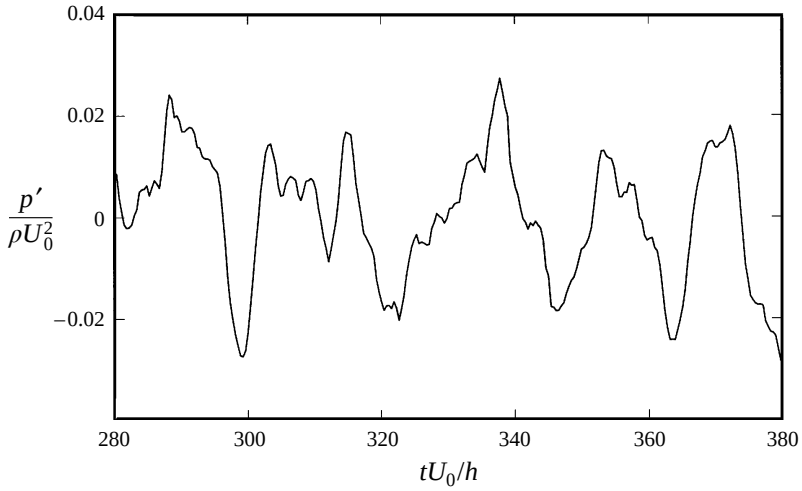

FIGURE 4. Spanwise-averaged pressure fluctuations at $x/h = 6.0$, $y/h = 0.055$.

the spanwise-averaged p' values. The time of the sudden drops of X_r in figure 3 corresponds to the p' minima in figure 4, indicating that the sudden drop is caused by the passage of the vortex centres. At instant when the passage of the turbulent vortices occurs, e.g. $t \approx 300h/U_0$, a single reattachment 'point' is not well defined; rather, small fragments of forward and reverse flow regions are scattered between $x/h \approx 5.0$ and $x/h \approx 7.5$. This cycle is repeated with $5h < X_r < 7.5h$. The sudden decrease in X_r following a slow increase was also speculated by Eaton & Johnston (1980). The formation and detachment from the step of large-scale vortices which cause the periodic movement of the reattachment location was also clearly illustrated in the two-dimensional simulation of the backward-facing step (Le & Moin 1994).

Similar oscillatory responses are also detected at other points in the flow field and in both vertical and streamwise velocity components. The Strouhal number corresponding to the dominant frequency is roughly $St = fh/U_0 \approx 0.06$, corresponding to period $T \approx 17h/U_0$. Eaton & Johnston (1980) measured the energy spectra of the streamwise velocity fluctuations (u') at several locations and reported that the spectral peak occurs in the Strouhal number range $0.066 < fh/U_0 < 0.08$. In recent numerical investigation of the coherent vortices behind a backward-facing step, Silveira Neto *et al.* (1993) found that the spectral peak of the streamwise turbulent intensity occurs at $St = 0.08$.

The motion of large-scale vortices can be traced by the contour plots of the spanwise-averaged pressure fluctuations in figure 5. Only the negative values are plotted for clarity. The vortices are generated at the step at approximately twice the frequency calculated above, and either dissipate or merge near the reattachment region. The resulting large vortex has a higher convection speed after the reattachment.

A spanwise cut through the flow at $x/h = 4.0$ (before the reattachment location) in figure 6 illustrates the high degree of three-dimensionality of the flow with several imbedded streamwise vortices. As expected, the most turbulent activities occur near reattachment. The flow is virtually quiet above $y/h = 2$. Silveira Neto *et al.* (1993) also found evidence for strong longitudinal vortices in the separated zone.

To examine the structural recovery to a normal turbulent boundary layer after reattachment, figure 7 presents the streamwise velocity (u') fluctuation contours in an

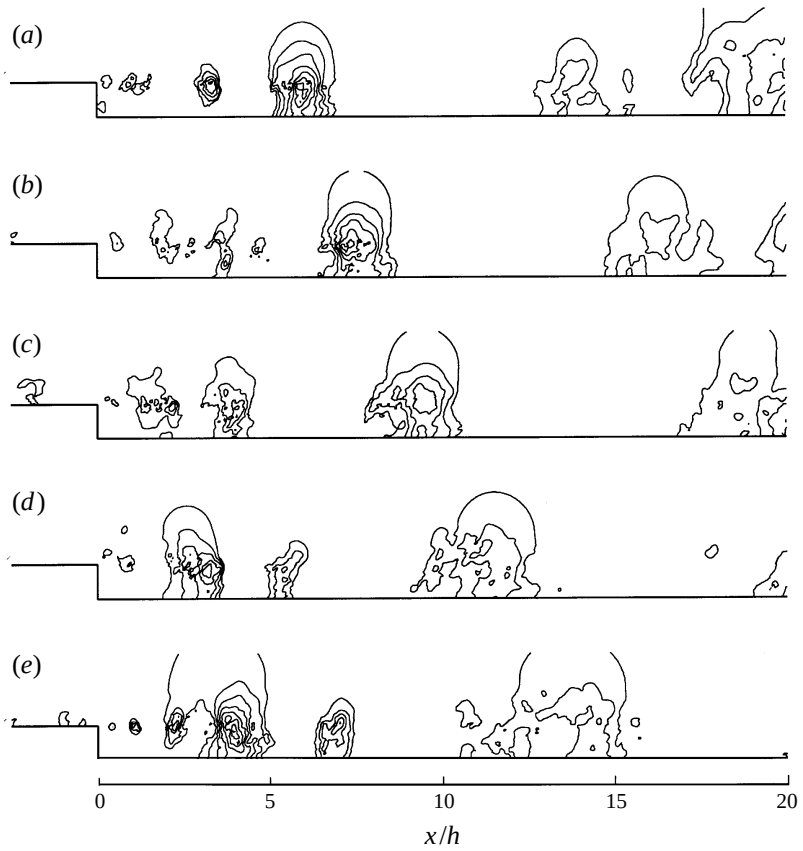

FIGURE 5. Spanwise-averaged pressure fluctuations as a function of time; negative contours. (*a*) $t = 299U_0/h$; (*b*) $t = 303U_0/h$; (*c*) $t = 306U_0/h$; (*d*) $t = 310U_0/h$; (*e*) $t = 314U_0/h$.

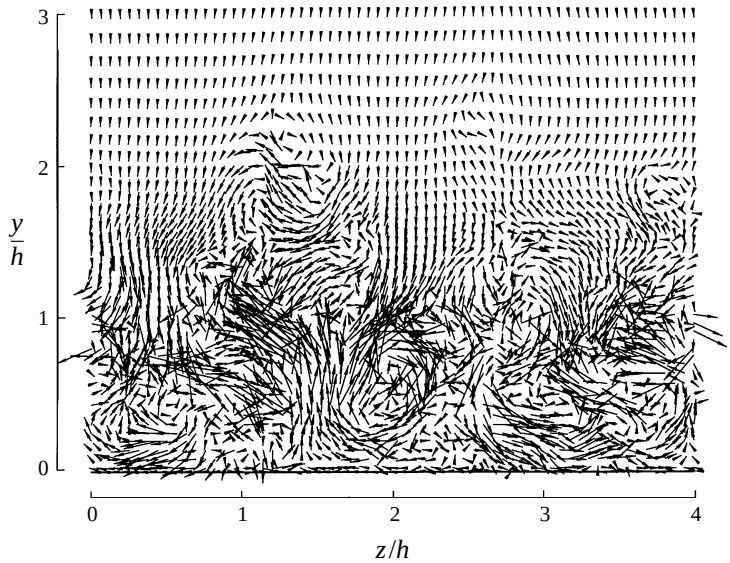

FIGURE 6. Instantaneous spanwise velocity vectors at $x/h = 4.0$.

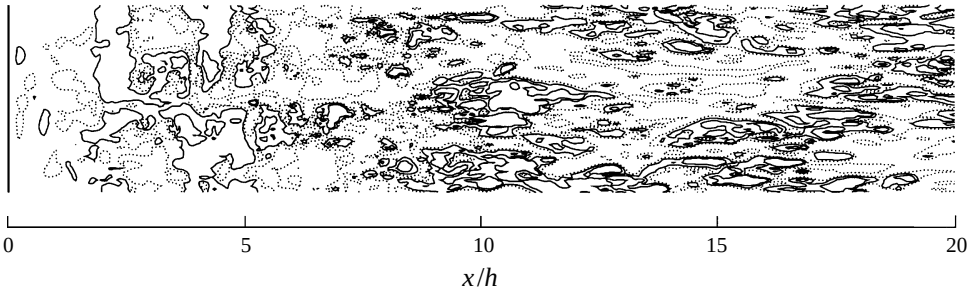

FIGURE 7. Instantaneous streamwise velocity fluctuations (u'/U_0) contours at $y^+ \approx 5$ (y^+ normalized to $u_\tau = 0.0384U_0$ at exit): ····· , negative; ——— , positive. Contours: −0.10, −0.02, 0.02, 0.10; $t = 382h/U_0$.

(x, z)-plane at $y^+ \approx 5$ (here y^+ was calculated using the shear velocity, $u_\tau = 0.038U_0$, at the exit). Near the exit, elongated, alternating positive and negative contour lines begin to appear. However, the wall streaks, characteristics of an attached turbulent boundary layer, are not yet present indicating that the flow has not fully recovered after 20 step heights.

3.2. *Reattachment length*

Four methods are used to determine the mean reattachment location, X_r: (*a*) by the location at which the mean velocity $U = 0$ at the first grid point away from the wall; (*b*) by the location of zero wall-shear stress ($\tau_w = 0$, or $\partial U/\partial y = 0$); (*c*) by the location of the mean dividing streamline ($\psi = 0$); and (*d*) by a p.d.f. method in which the mean reattachment point is indicated by the location of 50% forward flow fraction. The p.d.f. method was also used experimentally by Westphal *et al.* (1984) and Adams *et al.* (1984). The results of the first three methods are within 0.1% of each other, and about 2% different from the p.d.f. result. The mean reattachment length is 6.28*h*. (The reattachment length was reported in Le, Moin & Kim 1993 as $X_r = 6.0h$. However, the total simulation time at the date of that publication was only $t \approx 204h/U_0$.) The X_r measurements in the JD experiment vary between 6.0*h* and 6.1*h* (Jovic & Driver 1994). Thus, there is a variation of between 2% and 3% among all measured and computed X_r. The reattachment length was demonstrated by Kuehn (1980) to increase as the expansion ratio increases. Durst & Tropea (1981) compiled data from a number of experiments to show that the most dramatic change was in the range $1.10 < ER < 1.30$ where X_r varied from 5*h* to 7*h*. The X_r from the current simulation and JD experiment concur with these findings.

Figure 8 shows the streamlines of the mean flow. A large secondary bubble is evident in the step corner, extending to 1.76*h* in the *x*-direction, and 0.8*h* in the *y*-direction. Friedrich & Arnal (1990) reported that the instantaneous secondary recirculation regions are three-dimensional bubbles, located in the corner. In the current computations, the secondary recirculation extends across the entire span. Not seen in figure 8 is a third corner vortex (Moffatt 1964) of 0.042*h* in size.

3.3. *Coefficient of friction*

The wall skin-friction coefficient is normalized by the inlet velocity as follows:

$$C_f = \frac{\tau_w}{\frac{1}{2}\rho U_0^2}. \tag{3.1}$$

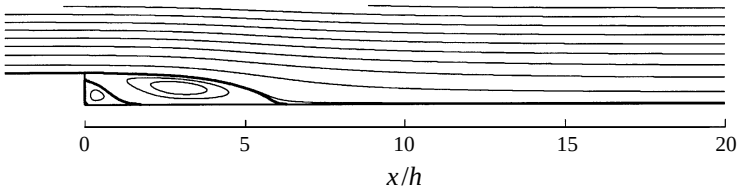

FIGURE 8. Contours of mean stream function ψ; reattachment length $X_r = 6.28h$.

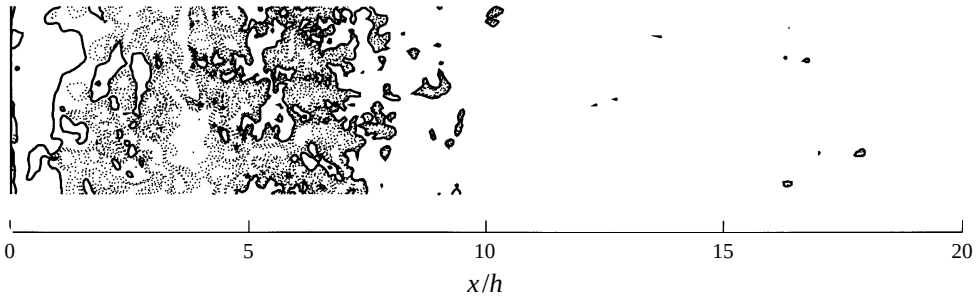

FIGURE 9. Instantaneous skin friction coefficient contours: ····· , negative C_f; ——, $C_f = 0$. $t = 300h/U_0$. Contours: −0.0005, −0.00075, −0.001, −0.002, −0.0025, −0.003.

Figure 9 shows instantaneous contours of C_f at the bottom wall. For clarity, only contours of negative C_f (reverse flow) are plotted. The heavy lines are the zero-friction lines separating the forward and backward moving flows near the wall. The instantaneous reattachment boundaries are a set of contorted lines. The lines of separation divide the flow domain near the wall into four general regions with alternating C_f signs: forward flow region (positive C_f, $x/h > 7.0$); reverse flow region (negative C_f, $2.5 < x/h < 5.0$); secondary bubble (positive C_f, $0.05 < x/h < 1.0$); and very close to the step, a weak second reverse flow region extending to only about $0.05h$. There are patches of positive C_f even in the reverse flow region which were also observed by Friedrich & Arnal (1990) in their LES results. Pockets of locally high $|C_f|$ values are seen with magnitudes up to several times the mean values.

The averaged C_f is compared with the JD data in figure 10. Excellent agreement is obtained between computational and experimental results. A striking departure from previous measurements is the large peak of negative skin friction in the recirculation region ($\approx -3 \times 10^{-3}$), seen in both computation and the JD experiment. Large negative C_f had been noted in previous backward-facing step experiments; the peak negative C_f here, however, is about 3 times larger than previously reported. Jovic & Driver (1995) also measured the skin friction in the reverse flow region for a wide range of Reynolds numbers. Their results show that the recirculation $|C_f|$ decreases in magnitude with increasing Reynolds number. The peak negative C_f reaches a value of approximately -1.0×10^{-3} at $Re_h \approx 20000$ which is the Reynolds number range used in many experiments. Thus, the large negative skin friction in the current study and in the JD experiment appears to be due to low Reynolds number effects. The low Reynolds number not only decreases the absolute value of the skin friction in the recirculation region, but also increases C_f in the recovery region.

In the recirculation region, Adams *et al.* (1984) proposed a (laminar) skin-friction law of the form $C_{f,U_N} \propto Re_N^{-1}$, where U_N is the maximum mean negative velocity which is realized at the distance N from the wall, C_{f,U_N} is the friction coefficient

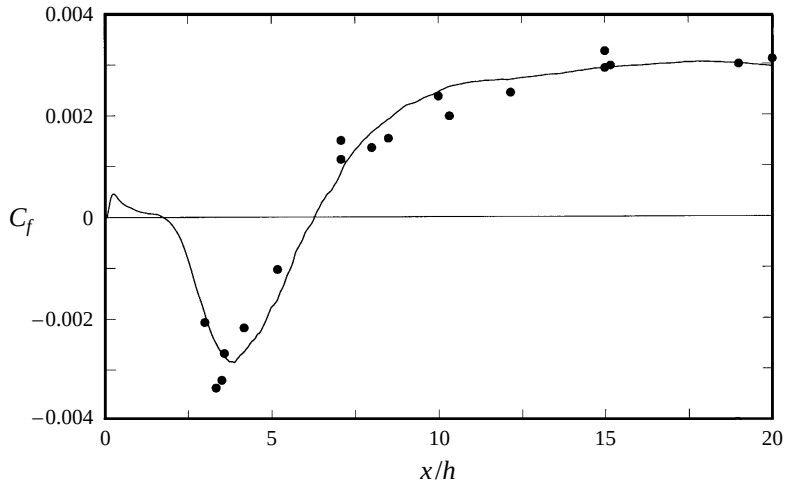

FIGURE 10. Comparison between computation and the JD step-wall skin friction coefficient: ———, computation; •, JD.

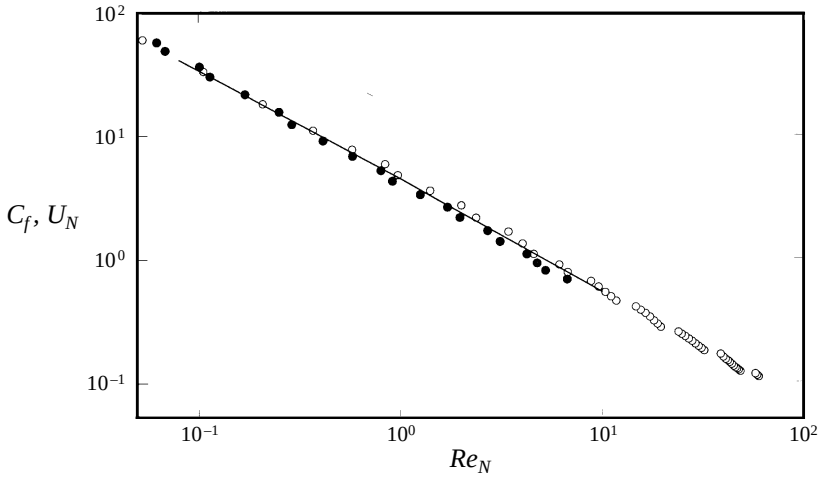

FIGURE 11. Skin friction in the recirculation region as a function of wall-layer Reynolds number: ○, primary vortex; •, secondary vortex; ———, $C_{f,U_N} = 4.5Re_N^{-0.92}$.

normalized by $\frac{1}{2}\rho U_N^2$, and Re_N is the Reynolds number based on U_N and N. Data from the current simulation are shown in figure 11. The data do not quite follow the -1 slope (≈ -0.92) but are much closer to the laminar relation than shown by Adams *et al.* (1984). The C_{f,U_N} correlation from the computational results is

$$C_{f,U_N} \approx 4.5Re_N^{-0.92}. \tag{3.2}$$

It should be noted in figure 11 that this relation also holds even for locations in the secondary vortex.

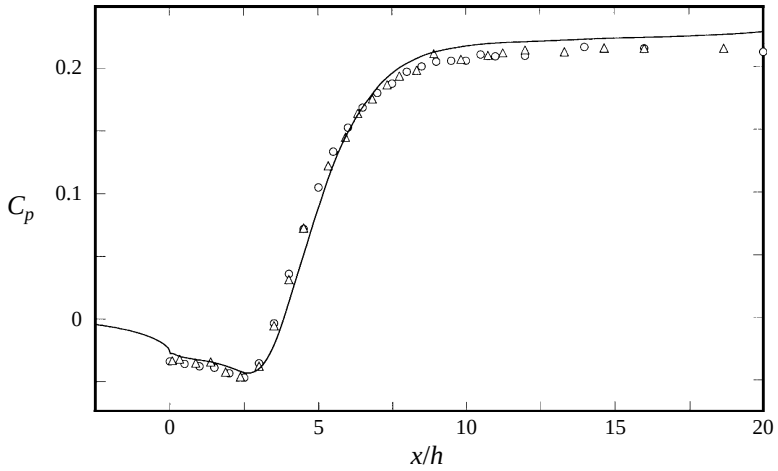

FIGURE 12. Comparison between computation and JD experiment step-wall pressure coefficient: ———, computation; ○, JD, bottom wall; △, JD, top wall.

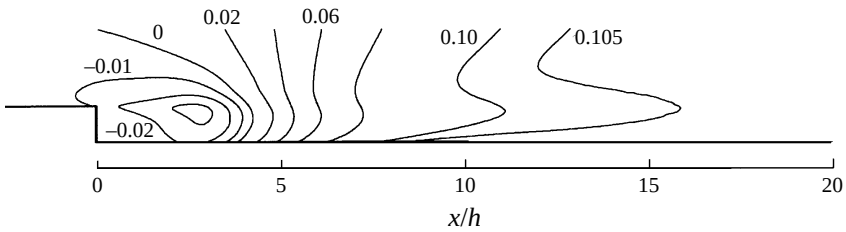

FIGURE 13. Contours of mean pressure, $(P - P_0)/\rho U_0^2$.

3.4. *Pressure distribution*

The pressure coefficient C_p is defined as

$$C_p = \frac{P - P_0}{\frac{1}{2}\rho U_0^2}, \tag{3.3}$$

where P_0 is a reference pressure. Figure 12 presents the C_p comparison between computation and JD data. Since the JD experiment has a double-expansion configuration, C_p values at both bottom and top walls are included in figure 12, showing symmetry in their experiment. The reference pressure P_0 is at $x/h = -5.0$ for both computation and the JD data. The agreement between computational and experimental results is excellent in the recirculation as well as reattachment regions; there is a small, but systematic, discrepancy in the recovery region. Other forms of C_p (e.g. Roshko & Lau 1965; Kim *et al.* 1978) that have been suggested to collapse the pressure data for various geometries and flows did not show a collapse of the present data and those from different flows (see Le & Moin 1994).

Figures 13 and 14 show the contours of P and $(\overline{p'^2})^{1/2}$. There is a slight favourable pressure gradient just prior to the step as indicated by the negative-P contour lines. The wall pressure fluctuations peak near the reattachment location and decrease downstream, an observation also made by Farabee & Casarella (1988). There is some evidence of the effect of the convective outflow condition on $(\overline{p'^2})^{1/2}$ near the exit.

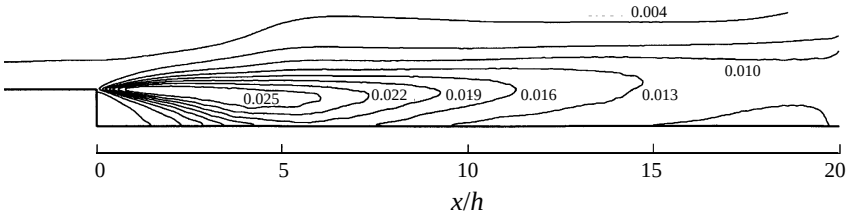

FIGURE 14. Contours of r.m.s. pressure fluctuations, $(\overline{p'^2})^{1/2}/\rho U_0^2$.

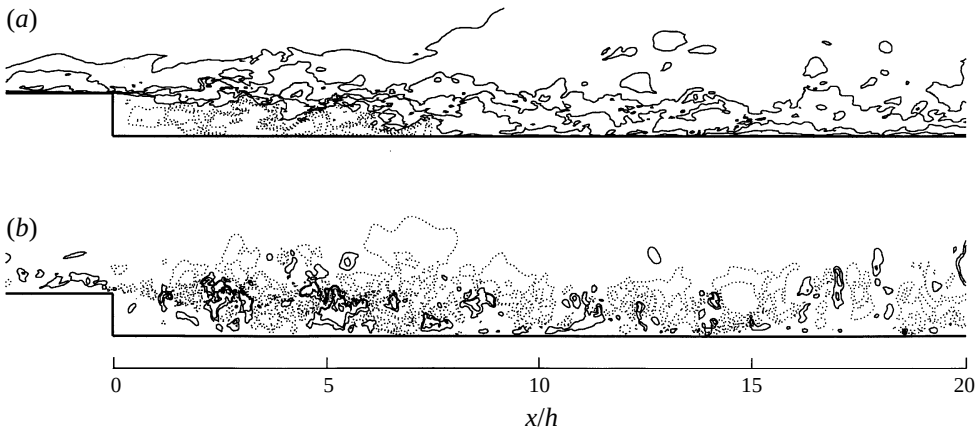

FIGURE 15. Instantaneous velocity contours: ····· , negative; ——, positive. (*a*) u/U_0, contours: −0.10, −0.05, −0.01, 0.10, 0.30, 0.50, 0.70, 0.90; (*b*) v/U_0, contours: −0.20, −0.10, −0.05, 0.05, 0.10, 0.20.

3.5. *Velocity*

The instantaneous contours of the velocity components in a typical (x, y)-plane are shown in figure 15. All velocities are normalized by the inlet free-stream velocity U_0. The negative contours are plotted with dotted lines and positive contours with solid lines. The streamwise velocity contours show a shear layer emanating from the step corner and reaching the bottom wall near $x/h = 8.0$. In figure 15(*b*), strong upward flow patches are concentrated within the shear layer inside the recirculation zone. The flow is mostly downward behind the reattachment, but alternating positive and negative v-contours are observed indicating the presence of spanwise vortices. High gradients are seen in both velocity components in the shear layer. Note that figure 15 is only representative of one vertical plane, and although contours of extreme values are omitted from the plots, numerical results indicate that the magnitude of each velocity component can reach values much higher than that shown in figure 15: $|u_{max}| \approx 1.3U_0$, and $|v_{max}| \approx 0.8U_0$. The maximum of v occurs near reattachment, where the downward moving fluid interacts with the wall. The streamwise velocity also reaches its maximum value near reattachment but in the free shear layer.

Figure 16 presents the comparison between computational results and the JD experiment for the mean streamwise velocity profiles. The comparison is made at four representative locations in the recirculation, reattachment and recovery regions. Excellent agreement between computational and experimental results is obtained at all locations.

The mean streamwise velocity profiles at x-stations throughout the domain behind

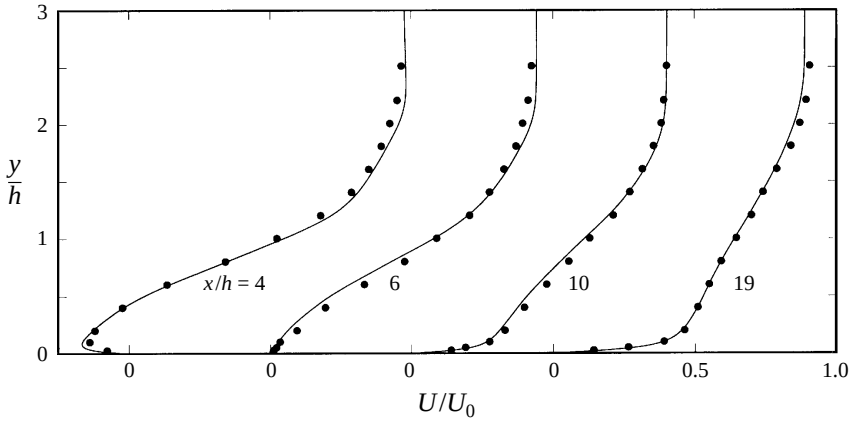

FIGURE 16. Comparison of mean streamwise velocity profiles: ———, computation; •, JD.

the step are shown in figure 17. In the recovery region, the velocity still has an inflection point at $x/h = 19.0$ indicating that an equilibrium boundary layer profile is not yet developed. Bradshaw & Wong (1972) observed profiles with an inflection point at 50 step heights downstream from the step.

Figure 18 shows the near-wall velocity profiles in the recovery region plotted in semi-logarithmic coordinates, and figure 19 compares the computational results with the JD measurements at $x/h = 19.0$. All profiles are below the universal log-law even at $20h$ downstream of the step. Previous experimental studies reported a recovery of the log-law profile as early as 6 step heights after the reattachment, e.g. Westphal *et al.* (1984), Kim *et al.* (1978), and Adams *et al.* (1984). The excellent agreement between the computation and JD profiles at $x/h = 19.0$ confirms that the deviation from the universal log-law is a real effect in this flow. The apparent discrepancy between the present near-wall profiles and previous experiments is attributed to the method of obtaining the wall-shear velocity u_τ. In previous experiments, the wall-shear velocity was calculated using the Clauser chart with the inherent assumption that the log-law of the zero-pressure-gradient turbulent boundary layer is applicable. The result was lower values of u_τ, hence higher u^+ values. The JD data in figure 19 were based on C_f directly measured by a laser interferometer, and not relying on the Clauser chart. In the present configuration, this discrepancy is as high as 17%, i.e. $u_\tau/u_{\tau_c} \approx 1.17$, where the subscript c denotes the value obtained using the Clauser chart.

The deviation of the velocity profile from the log-law appears to be a result of the strong streamwise adverse pressure gradient (APG) which is experienced by the flow following the sudden expansion. Although the effect of APG on boundary layers has been studied by many authors, the universal log-law has been considered applicable because of the use of the Clauser chart as mentioned above. A re-evaluation of the applicability of the log-law in non-zero-pressure-gradient flows was recently conducted by Nagano, Tagawa & Tsuji (1991). They concluded that the mean velocity profile does indeed shift downward from the standard log-law in an APG. Studies by Driver (1991) of flows with APG also support this finding.

Since u_τ is proportional to $C_f^{1/2}$, and as shown earlier, the calculated C_f in the recovery region is high due to low Reynolds number effects, the profile of U/u_τ in wall coordinates is further depressed below the universal log-law. Therefore, APG

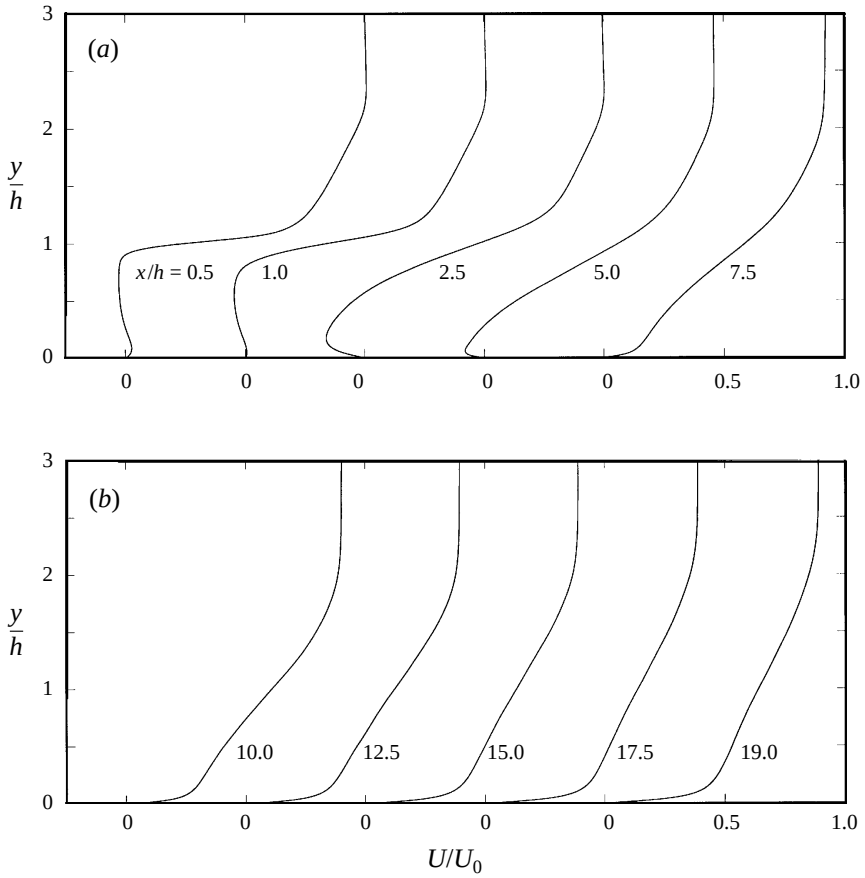

FIGURE 17. Mean streamwise velocity profiles. (*a*) Recirculation and reattachment regions; (*b*) recovery region.

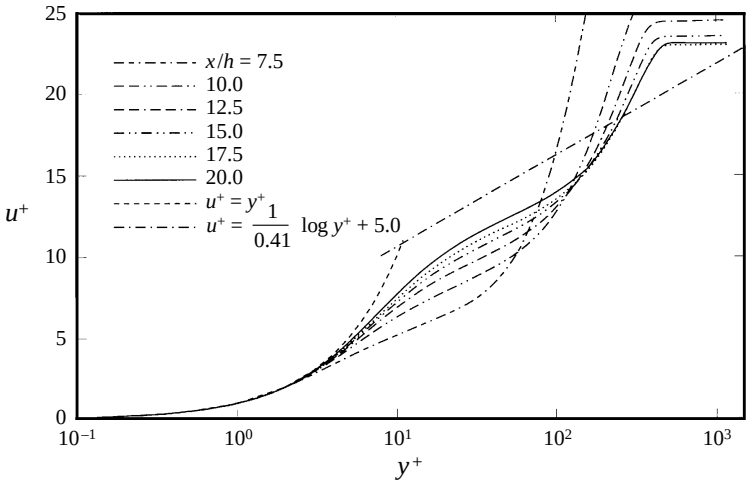

FIGURE 18. Mean streamwise velocity profiles in wall coordinates.

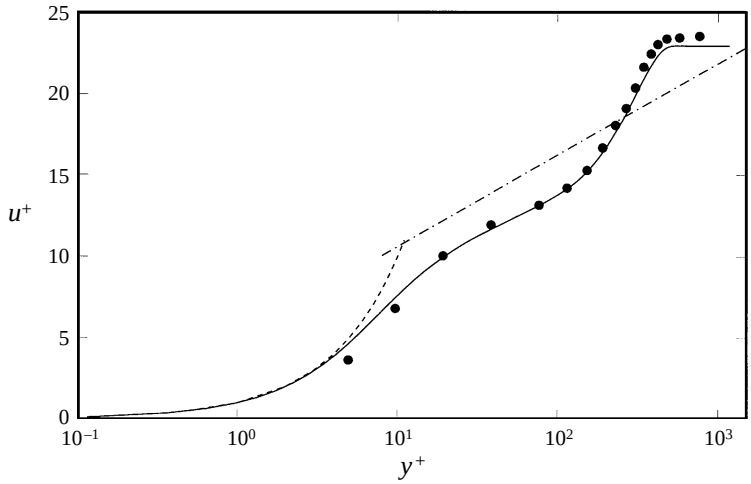

FIGURE 19. Mean streamwise velocity profiles in wall coordinates at $x/h = 19.0$: – – – – , $u^+ = y^+$; —·—, $u^+ = \frac{1}{0.41}\log y^+ + 5.0$; ———, computation; •, JD.

alone does not fully account for the departure from the log-law, but the low Reynolds number also appears to have an effect on the rate of approach to recovery.

In the recirculation, the law of the wall for attached flows does not hold. The backflow appears to behave more like a laminar flow (Adams *et al.* 1984). Simpson (1983) suggested the following empirical relation for the overlap layer ($0.02 < y/N < 1$):

$$\frac{U}{|U_N|} = A\left[\frac{y}{N} - \log\left(\frac{y}{N}\right) - 1\right] - 1, \tag{3.4}$$

where N is the distance from the wall to the maximum mean negative velocity, U_N, and the constant A was selected to be 0.3 based on Simpson *et al.*'s (1990) data. Adams *et al.* (1984) applied this relation to their backward-facing step data, but (3.4) did not provide a good representation of their data. Figure 20 presents the velocity profiles at three locations in the recirculation zone, plotted in the coordinates suggested by Simpson *et al.* (1990). Also plotted for comparison is the relation in (3.4). Simpson's (1983) correlation with $A = 0.3$ deviates from the computed profiles by as much as 45% in the overlap layer ($0.02 < y/N < 1$). An adequate collapse is seen for locations in the range $3 < x/h < 5$. The similarity does not hold as one moves closer to the zero-velocity points (reattachment, $x/h = 6.28$, and secondary bubble, $x/h = 1.74$).

3.6. *Turbulence intensities and Reynolds shear stresses*

Figure 21 shows the instantaneous velocity fluctuations. Again, contours of extreme values are omitted. Examinations of the instantaneous velocities at different time steps show that $|u'|$, $|v'|$ and $|w'|$ can reach as high as $0.4U_0$, $0.6U_0$ and $1.0U_0$, respectively, near the reattachment. The high value of $|w'|_{max}$ near reattachment is a bit surprising, but appears to be physical. A cursory investigation of a single field in a confined co-annular jet flow (Akselvoll & Moin 1996) also revealed large transverse velocities ($|w'|_{max} \approx 0.8$). It appears that the fluctuations in the backflow region are relatively small (the maximum value of velocity fluctuations in this region is approximately $0.08U_0$). However, considering that the maximum mean streamwise velocity in this region is only $U_N \approx 0.18U_0$, the fluctuations can reach 40% of U_N.

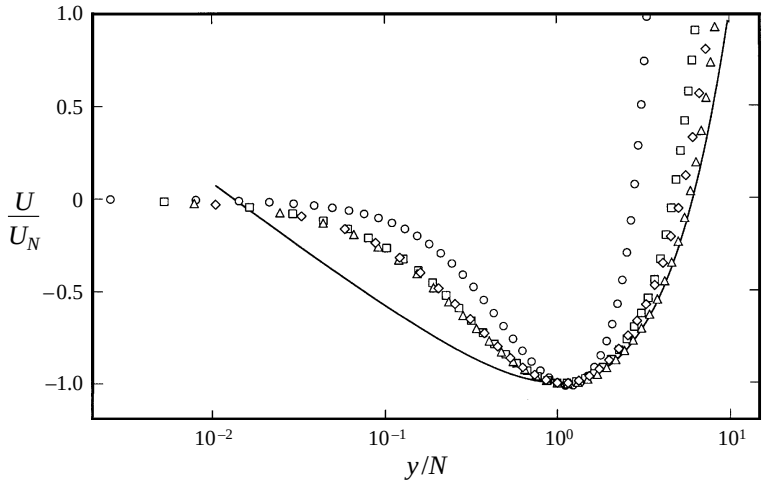

FIGURE 20. Normalized recirculation mean velocity profiles, U/U_N versus y/N: ○, $x/h = 2.0$; □, $x/h = 3.0$; △, $x/h = 4.0$; ◇, $x/h = 5.0$; ———, Simpson's (1983) model with $A = 0.3$.

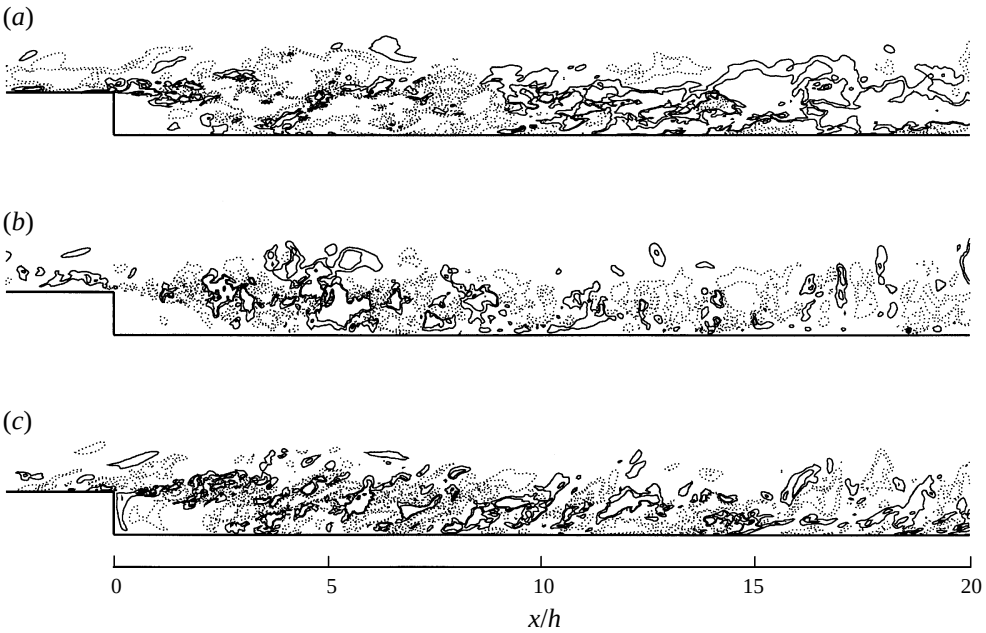

FIGURE 21. Instantaneous velocity fluctuation contours: ·····, negative; ———, positive. Contours: −0.10, −0.05, 0.05, 0.10. (*a*) u'/U_0; (*b*) v'/U_0; (*c*) w'/U_0.

This is in accordance with Westphal *et al.*'s (1984) suggestion that the reverse flow is lamilar-like but with high unsteadiness imposed by the turbulent shear layer.

The rms profiles of the longitudinal and vertical velocity fluctuations ($(\overline{u'^2})^{1/2}$, $(\overline{v'^2})^{1/2}$), and the Reynolds shear stress component ($\overline{u'v'}$) are compared with the JD results at four streamwise locations in figure 22. The agreement between computation and the JD results is excellent for all Reynolds stress components. Just after the reattachment zone, the near-wall peak in the JD streamwise turbulence intensity appears to develop earlier than in the computation ($x/h = 10.0$).

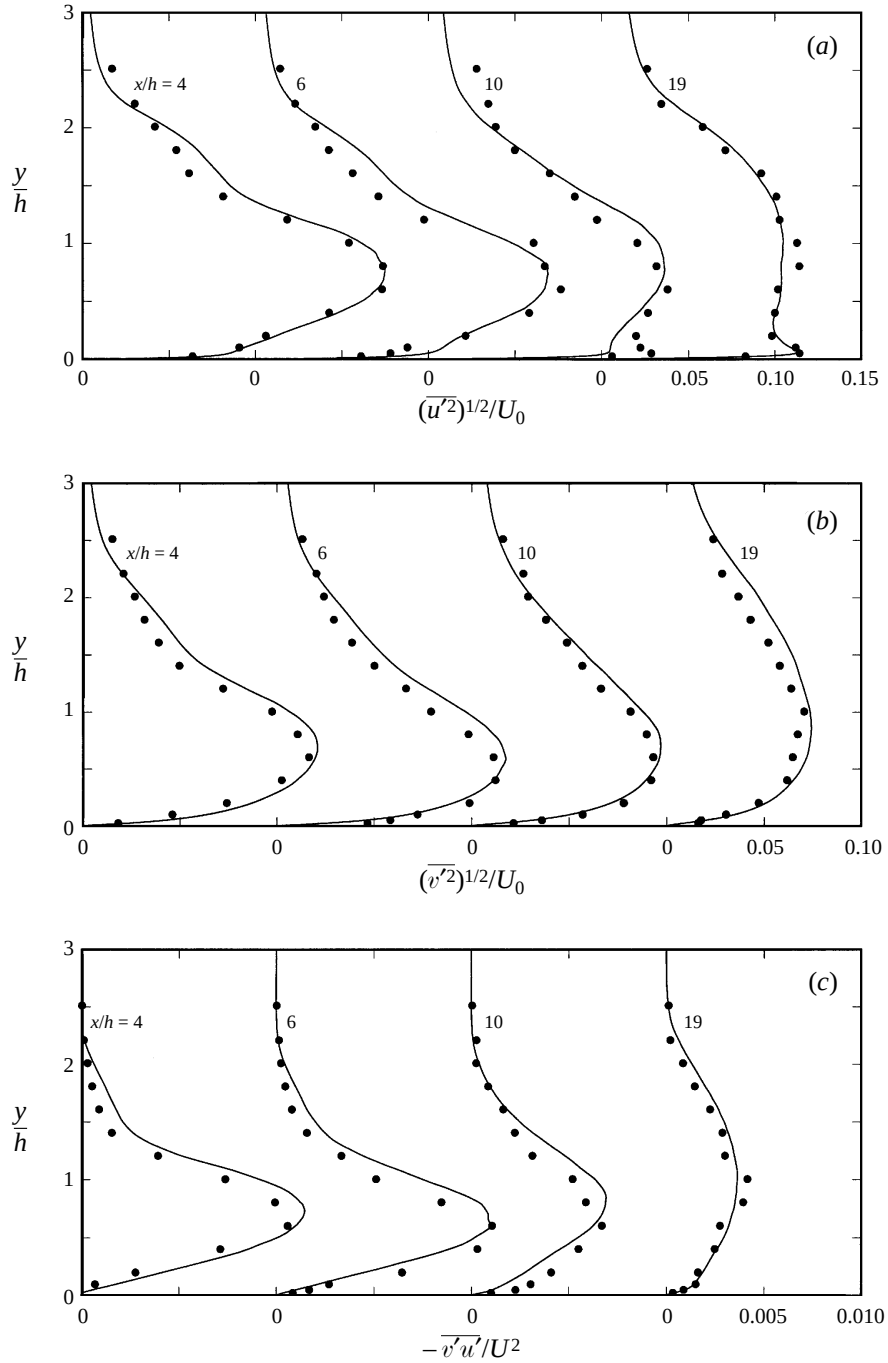

FIGURE 22. Comparison of Reynolds stress profiles: ———, computation; •, JD. (*a*) $(\overline{u'^2})^{1/2}/U_0$; (*b*) $(\overline{v'^2})^{1/2}/U_0$; (*c*) $-\overline{u'v'}/U_0^2$.

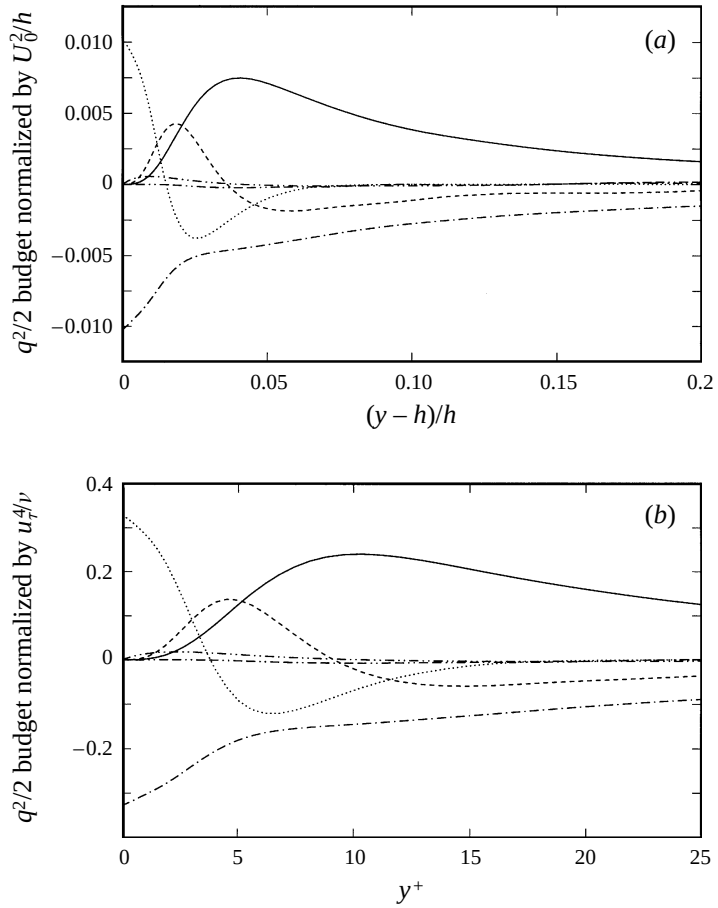

FIGURE 23. Turbulent kinetic energy budget at $x/h = -2.0$: – – ··, convection; ———, production; – – – –, turbulence transport; ·····, viscous diffusion; —·—, viscous dissipation; —··—, velocity–pressure gradient. (*a*) Away from the wall; (*b*) near the wall.

3.7. *Turbulent kinetic energy budget*

The turbulent kinetic energy budget is given by

$$\frac{\partial(\frac{1}{2}q^2)}{\partial t} = \underbrace{-\tfrac{1}{2}U_k\overline{(u_l'u_l')}_{,k}}_{C_k} \underbrace{-\overline{u_l'u_k'}U_{l,k}}_{P_k} \underbrace{-\tfrac{1}{2}\overline{(u_l'u_l'u_k')}_{,k}}_{T_k} + \underbrace{\frac{1}{2Re}\overline{(u_l'u_l')}_{,kk}}_{D_k} \underbrace{-\frac{1}{Re}\overline{u_{l,k}'u_{l,k}'}}_{\epsilon_k} \underbrace{-\overline{u_l'p_{,l}'}}_{\Pi_k}, \tag{3.5}$$

where

$$\tfrac{1}{2}q^2 = \tfrac{1}{2}(\overline{u'^2} + \overline{v'^2} + \overline{w'^2}). \tag{3.6}$$

The terms on the right hand side of (3.5) are identified as follows:
C_k = convection, P_k = production, T_k = turbulence transport, D_k = viscous diffusion, ϵ_k = viscous dissipation, Π_k = velocity–pressure gradient.

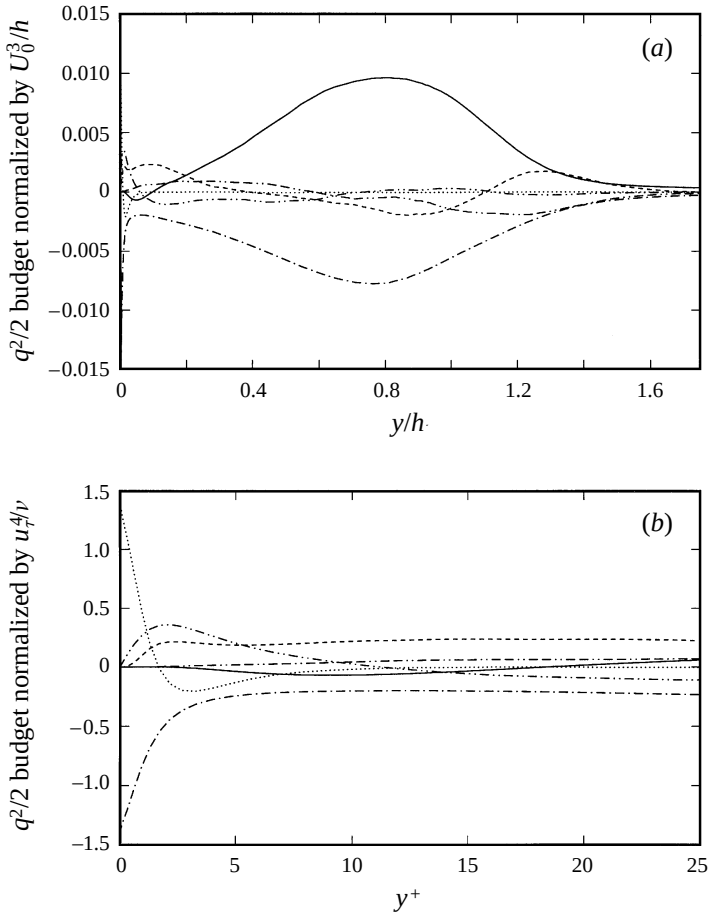

FIGURE 24. Turbulent kinetic energy budget as figure 23 but at $x/h = 4.0$.

The budgets for the turbulent kinetic energy are shown in figures 23–26. At two step heights before the separation, the energy budget (figure 23) is similar to that of a zero-pressure-gradient turbulent boundary layer (Spalart 1988) although there is an enhancement of the viscous terms near the wall (as in the longitudinal turbulence intensity) and also higher levels of turbulence transport.

In the recirculation region, P_k is mostly due to the production of the longitudinal stress, P_{11}. The turbulence transport term removes energy from the shear layer region, $0.3 < y/h < 1.1$, and delivers it to regions near the wall and away from the shear layer.

The turbulent kinetic energy budget in the recirculation region is very similar to that of a plane mixing layer (Bradshaw & Ferriss 1965 and Roger & Moser 1993). The presence of the 'ground' does not affect the basic structure of the shear layer emanating from the step (Hunt 1990). This budget also agrees qualitatively with the measurements by Chandrsuda & Bradshaw (1981) for a backward-facing step flow. Both production P_k and viscous dissipation ϵ_k have maxima at the same point in the free-shear layer. The peak ϵ_k is approximately 60% of the production peak. Thus, the commonly used assumption leading to eddy viscosity parameterization, that production is balanced with dissipation, is not applicable in the recirculation region.

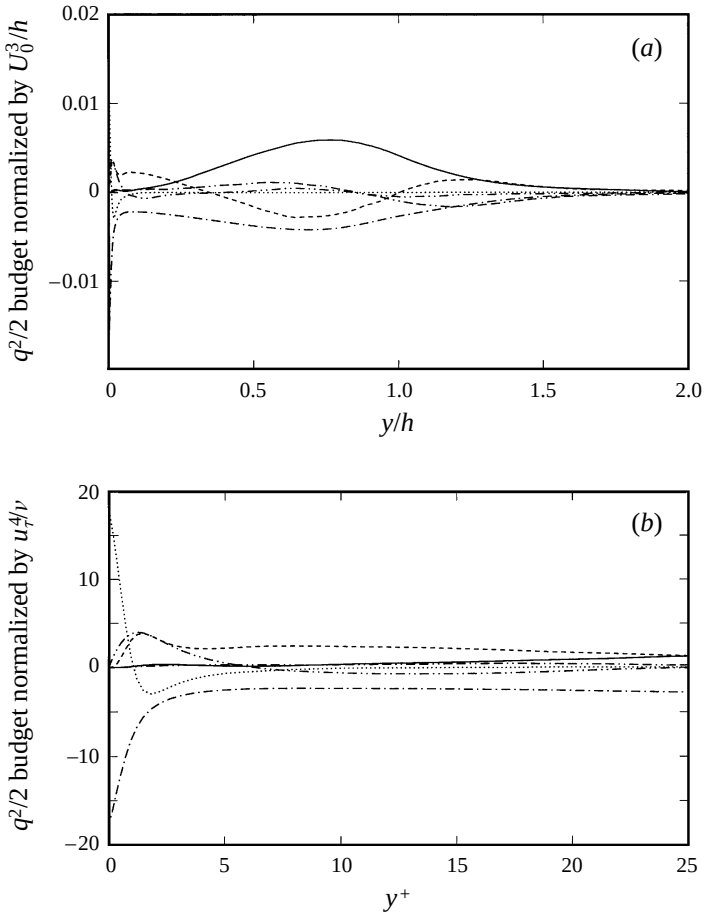

FIGURE 25. Turbulent kinetic energy budget as figure 23 but at $x/h = 7.0$.

As one approaches the wall, production becomes a consuming term because of the negative gradient of the mean reverse flow (figure 24*b*), although its magnitude is relatively small. Very close to the wall, the two viscous terms, D_k and ϵ_k, grow rapidly (their value at the wall is about 40% higher than the peak production in the shear layer). The velocity–pressure gradient is very significant in the region $y^+ < 10$ where it balances the dissipation and turbulence transport terms.

All terms decay with x except near the wall. Near the flow exit, $x/h = 18$, the turbulent kinetic energy budget resembles that of a turbulent boundary layer. However, the effects of the free-shear layer are still present, e.g. T_k is still large at $y/h = 1$. The relative magnitudes of the viscous terms near the wall are much larger than in a zero-pressure-gradient boundary layer.

The budget of the Reynolds shear stress, $\overline{u'v'}$ is shown in figure 27 for locations near the reattachment. In the recirculation region (figure 27*a*), the production is dominant and peaks in the shear layer. The velocity–pressure gradient term also peaks in the shear layer, but only accounts for about 75% of the production, P_{12}. As the flow progresses downstream through the reattachment zone, the production and velocity–pressure gradient are still dominant, but profile peaks shift from the shear layer to the wall region.

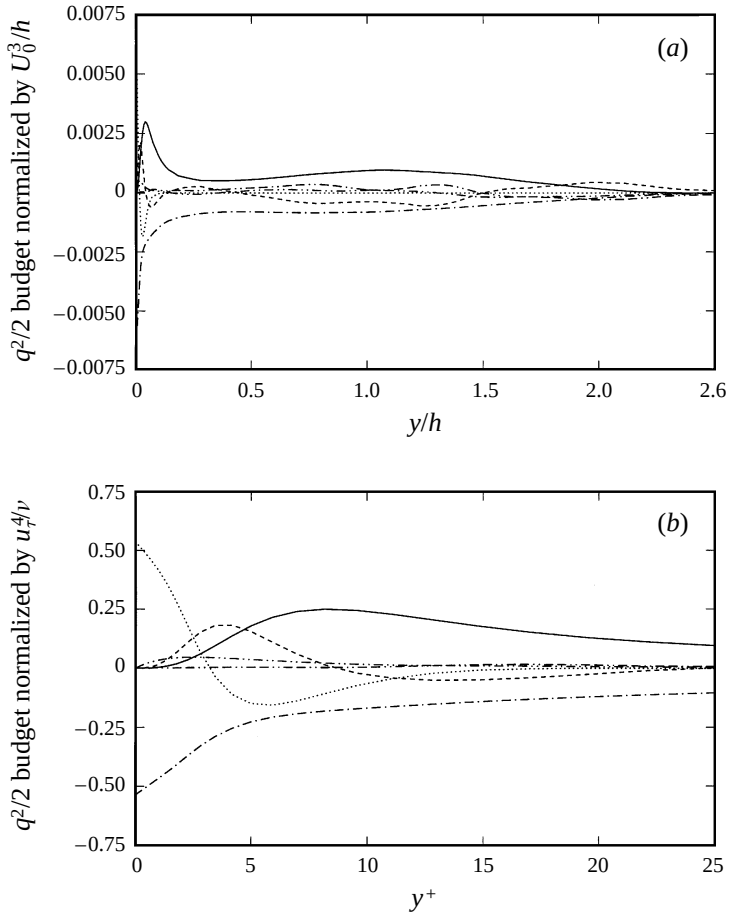

FIGURE 26. Turbulent kinetic energy budget as figure 23 but at $x/h = 18.0$.

The reader is referred to Le & Moin (1994) for complete budgets of the Reynolds stress components.

4. Conclusions

A direct numerical simulation of a turbulent flow over a backward-facing step was performed.

Examination of the spanwise-averaged reattachment length shows quasi-periodic behaviour with Strouhal number $St \approx 0.06$ which is in accordance with previous experimental deductions that such motions exist in the backward-facing step flow. The flow also exhibits strong streamwise vortical structures.

Statistical results show excellent agreement with data from the concurrent experiment by Jovic & Driver (1994). The mean reattachment length X_r is 6.28 step heights from the separation which agrees to within 3% of Jovic & Driver's (1994) measurements. In the low Reynolds number range considered in this study, large negative skin friction is observed in the recirculation region. The peak negative C_f is approximately 3 times larger than the values measured in experiments with higher Reynolds numbers ($Re_h \approx 30000$). Higher skin friction is also seen in the recovery

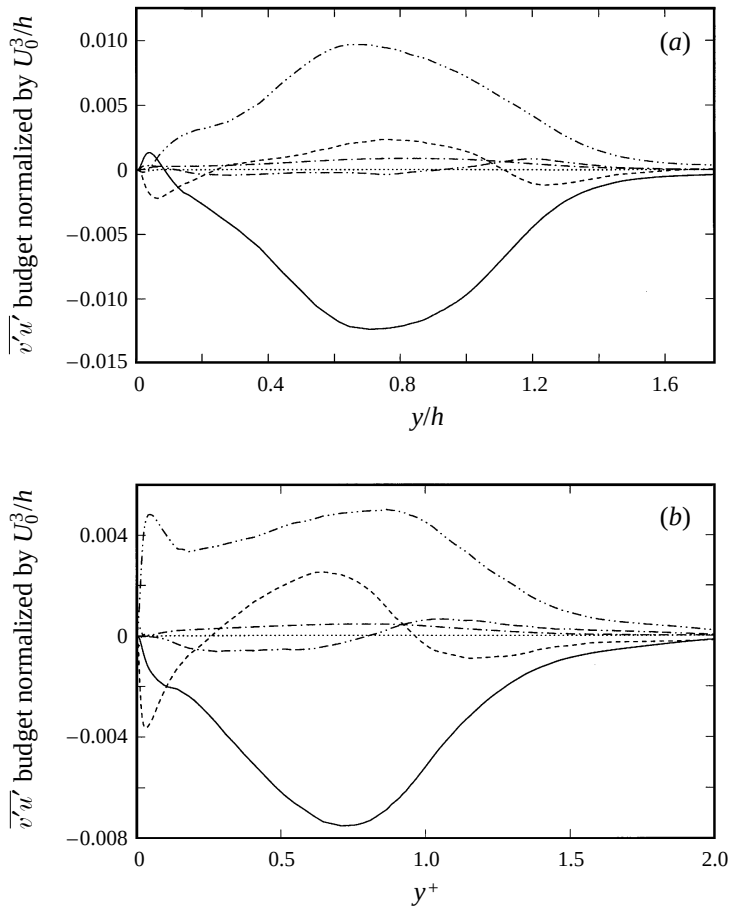

FIGURE 27. Reynolds shear stress budget near reattachment: – – ··, convection; ———, production; – – – –, turbulence transport; ·····, viscous diffusion; —·—, viscous dissipation; —··—, velocity–pressure gradient. (*a*) $x/h = 4.0$ (least-square fit); (*b*) $x/h = 7.0$ (least-square fit).

region. Additional experiments by Jovic & Driver (1995) with varying Reynolds numbers confirm that the high skin friction in the recirculation zone is due to the low Reynolds number effects.

In the recovery region, contrary to reports by previous experiments, both DNS and JD mean velocity profiles indicate a shift downward from the universal log-law. The intercept C of the logarithmic profile is about 2.54 compared to 5.0 of the universal log-law. Based on recent studies of turbulent flows under adverse pressure gradients (Nagano *et al.* 1991; Driver 1991), it can be concluded that the deviation from the universal log-law in the recovery region is due to the combined effects of the low Reynolds number and adverse pressure gradient.

The budgets of all components of the Reynolds stress tensor were computed. Up to third-order statistics are documented in a database allowing evaluation of the budgets at all locations in the flow field. The turbulent kinetic energy budget in the recirculation region is similar to that of a turbulent mixing layer. In the shear layer, the peak energy production and dissipation are near the step, $y/h \approx 1$. The peak dissipation is approximately 60% of the peak turbulent production. The turbulence diffusion is a consuming term in the range $0.3 < y/h < 1$ but becomes a 'producing'

term outside this range. The velocity–pressure gradient and viscous diffusion are negligible in the shear layer, but both are significant in the near-wall region. Near the domain exit ($x/h = 20$), the energy budget still shows a strong effect of the shear layer near $y/h = 1$, indicating that the flow has not fully recovered.

This work was supported by the Center for Turbulence Research at NASA-Ames and Stanford University, by the Office of Naval Research and by the National Science Foundation.

REFERENCES

Adams, E. W. & Johnston, J. P. 1985 Experimental studies of high Reynolds number backward-facing step flow. In *Proc. Fifth Intl Symp. on Turbulent Shear Flows, Cornell University*, pp. 5.1–5.6.

Adams, E. W., Johnston, J. P. & Eaton, J. K. 1984 Experiments on the structure of turbulent reattaching flow. *Rep.* MD-43. Thermosciences Division, Dept. of Mech. Engng, Stanford University.

Akselvoll, K. & Moin, P. 1996 Large-eddy simulation of turbulent confined coannular jets. *J. Fluid Mech.* **315**, 387–411.

Armaly, B. F., Durst, F., Pereira, J. C. F. & Schönung, B. 1983 Experimental and theoretical investigation of backward-facing step. *J. Fluid Mech.* **127**, 473–496.

Bradshaw, P. & Ferriss, D. H. 1965 The spectral energy balance in a turbulent mixing layer. *AERO Rep.* 1144. National Physical Laboratory, England.

Bradshaw, P. & Wong, F. Y. F. 1972 The reattachment and relaxation of a turbulent shear layer. *J. Fluid Mech.* **52**, 113–135.

Chandrsuda, C. & Bradshaw, P. 1981 Turbulence structure of a reattaching mixing layer. *J. Fluid Mech.* **110**, 171–194.

Driver, D. M. 1991 Reynolds shear stress measurements in a separated boundary layer flow. *AIAA Paper* 91-1787.

Driver, D. M. & Seegmiller, H. L. 1985 Features of a reattaching turbulent shear layer in divergent channel flow. *AIAA J.* **23**, 163–171.

Driver, D. M., Seegmiller, H. L. & Marvin, J. 1983 Unsteady behavior of a reattaching shear layer. *AIAA Paper* 83-1712.

Driver, D. M., Seegmiller, H. L. & Marvin, J. 1987 Time-dependent behavior of a reattaching shear layer. *AIAA J.* **25**, 914–919.

Durst, F. & Pereira, J. C. F. 1988 Time-dependent laminar backward-facing step flow in a two-dimensional duct. *Trans. ASME J. Fluids Engng* **110**, 289–296.

Durst, F. & Tropea, C. 1981 Turbulent, backward-facing step flows in two-dimensional ducts and channels. In *Proc. Third Intl Symp. on Turbulent Shear Flows, University of California, Davis*, pp. 18.1–18.5.

Eaton, J. K. & Johnston, J. P. 1980 Turbulent flow reattachment: An experimental study of the flow and structure behind a backward-facing step. *Rep.* MD-39. Thermosciences Division, Dept. of Mech. Engng, Stanford University.

Farabee, T. M. & Casarella, M. J. 1988 Wall pressure fluctuations beneath a disturbed turbulent boundary layer. *Intl Symp. on Flow Induced Vibration and Noise: Acoustic Phenomena and Interaction in Shear Flows over Compliant and Vibrating Surfaces, New York* (ed. M. P. Paidoussis), pp. 121–135. ASME.

Friedrich, R. & Arnal, M. 1990 Analysing turbulent backward-facing step flow with the lowpass-filtered Navier–Stokes equations. *J. Wind Engng Indust. Aerodyn* **35**, 101–128.

Gresho, P. M., Gartling, D. K., Cliffe, K. A., Garratt, T. J., Spence, A., Winters, K. H., Goodrich, J. W. & Torczynski, J. R. 1993 Is the steady viscous incompressible two-dimensional flow over a backward-facing step at $Re = 800$ stable? *Intl J. Numer. Meth. Fluids* **17**, 501–541.

Harlow, F. H. & Welch, J. E. 1965 Numerical calculation of time-dependent viscous incompressible flow of fluid with free surface. *Phys. Fluids* **8**, 2182–2189.

HUNT, J. C. R. 1990 Numerical simulation of unsteady flows and transition to turbulence. *Proc. ERCOFTAC Workshop held at EPFL, March 26–28, Lausanne, Switzerland* (ed. O. Pironneau, W. Rodi, I. L. Ryhming, A. M. Savill & T. V. Truong). Cambridge University Press.

ISOMOTO, K. & HONAMI, S. 1989 The effect of inlet turbulence intensity on the reattachment process over a backward-facing step. *Trans. ASME J. Fluids Engng* **111**, 87–92.

JOVIC, S. & DRIVER, D. M. 1994 Backward-facing step measurement at low Reynolds number, $Re_h = 5000$. *NASA Tech. Mem.* 108807.

JOVIC, S. & DRIVER, D. M. 1995 Reynolds number effects on the skin friction in separated flows behind a backward facing step. *Exps. Fluids* **18**, 464–467.

KAIKTSIS, L., KARNIADAKIS, G. E. & ORSZAG, S. A. 1991 Onset of three-dimensionality, equilibria, and early transition in flow over a backward-facing step. *J. Fluid Mech.* **231**, 501–528.

KIM, J., KLINE, S. J. & JOHNSTON, J. P. 1978 Investigation of separation and reattachment of a turbulent shear layer: Flow over a backward-facing step. *Rep.* MD-37. Thermosciences Division, Dept. of Mech. Engng, Stanford University.

KIM, J. & MOIN, P. 1985 Application of a fractional-step method to incompressible Navier-Stokes equations. *J. Comput. Phys.* **59**, 308–323.

KUEHN, D. M. 1980 Some effects of adverse pressure gradient on the incompressible reattaching flow over a rearward-facing step. *AIAA J.* **18**, 343–344.

LE, H. & MOIN, P. 1991 An improvement of fractional step methods for the incompressible Navier-Stokes equations. *J. Comput. Phys.* **92**, 369–379.

LE, H. & MOIN, P. 1994 Direct numerical simulation of turbulent flow over a backward-facing step. *Rep.* TF-58. Thermosciences Division, Dept. of Mech. Engng, Stanford University.

LE, H., MOIN, P. & KIM, J. 1993 Direct simulations of turbulent flow over a backward-facing step. *Proc. Ninth Symp. on Turbulent Shear Flows, Kyoto University*, pp. 13-2-1–13-2-5.

LEE, S., LELE, S. K. & MOIN, P. 1992 Simulation of spatially evolving turbulence and the applicability of Taylor's hypothesis in compressible flow. *Phys. Fluids* A **4**, 1521–1530.

LOWERY, P. S. & REYNOLDS, W. C. 1986 Numerical simulation of a spatially-developing, forced, plane mixing layer. *Rep.* TF-26. Thermosciences Division, Dept. of Mech. Engng, Stanford University.

MOFFATT, M. K. 1964 Viscous and resistive eddies near a sharp corner. *J. Fluid Mech.* **18**, 1–18.

NAGANO, Y., TAGAWA, M. & TSUJI, T. 1991 Effects of adverse pressure gradients on mean flows and turbulence statistics in a boundary layer. *Proc. Eighth Symp. on Turbulent Shear Flows, Technical University of Munich*, pp. 2-3-1–2-3-6.

ÖTÜGEN, M. V. 1991 Expansion ratio effects on the separated shear layer and reattachment downstream of a backward-facing step. *Exps. Fluids* **10**, 273–280.

PAULEY, L. L., MOIN, P. & REYNOLDS, W. C. 1988 A numerical study of unsteady laminar boundary layer separation. *Rep.* TF-34. Thermosciences Division, Dept. of Mech. Engng, Stanford University.

RA, S. H. & CHANG, P. K. 1990 Effects of pressure gradient on reattaching flow downstream of a rearward-facing step. *J. Aircraft* **27**, 93–95.

ROGERS, M. & MOSER, R. 1993 Direct simulations of a self similar turbulent mixing layer. *Phys. Fluids* A **6**, 903–923.

ROSHKO, A. & LAU, J. C. 1965 Some observations on transition and reattachment of a free shear layer in incompressible flow. *Proc. 1965 Heat Transfer and Fluid Mechanics Institute,* pp. 157–167. Stanford University Press.

SCHUMANN, U. & SWEET, R. A. 1988 Fast Fourier transforms for direct solution of Poisson's equation with staggered boundary conditions. *J. Comput. Phys.* **75**, 123–137.

SILVEIRA NETO, A., GRAND, D., METAIS, O. & LESIEUR, M. 1993 A numerical investigation of the coherent vortices in turbulence behind a backward-facing step. *J. Fluid Mech.* **256**, 1–25.

SIMPSON, R. L. 1983 A model for the backflow mean velocity profile. *AIAA J.* **21**, 142–143.

SIMPSON, R. L., AGARWAL, N. K., NAGABUSHANA, K. A. & OLCMEN, S. 1990 Spectral measurements and other features of separating turbulent flows. *AIAA J.* **28**, 446–452.

SINHA, S. N., GUPTA, A. K. & OBERAI, M. M. 1981 Laminar separating flow over backsteps and cavities part I: backsteps. *AIAA J.* **19**, 1527–1530.

SPALART, P. R. 1987 Hybrid RKW3 + Crank-Nicolson scheme. Private communication, NASA-Ames Research Center, Moffett Field, CA.

Spalart, P. R. 1988 Direct simulation of a turbulent boundary layer up to $R_\theta = 1410$. *J. Fluid Mech.* **187**, 61–98.

Spalart, P. R., Moser, R. D. & Rogers, M. M. 1991 Spectral methods for the Navier–Stokes equations with one infinite and two periodic directions. *J. Comput. Phys.* **96**, 297–324.

Westphal, R. V., Johnston, J. P. & Eaton, J. K. 1984 Experimental study of flow reattachment in a single-sided sudden expansion. *Rep.* MD-41. Thermosciences Division, Dept. of Mech. Engng, Stanford University.